High-Aspect-Ratio Metal Microfabrication by Nickel Electroplating of Patterned Carbon Nanotube Forests

Lawrence Barrett

A senior thesis submitted to the faculty of
Brigham Young University
in partial fulfillment of the requirements for the degree of

Bachelor of Science

Robert Davis, Advisor

Department of Physics and Astronomy

Brigham Young University

August 2014

ABSTRACT

High-Aspect-Ratio Metal Microfabrication by Nickel Electroplating of Patterned Carbon Nanotube Forests

Lawrence Barrett
Department of Physics and Astronomy
Bachelor of Science

High-aspect-ratio metallic microstructures have a variety of potential applications in sensing and actuation. However, fabrication remains a challenge. We have fabricated Ni microstructures with over 20:1 aspect ratios by electroplating patterned, carbon-coated, carbon-nanotube forests (CNTs) using a nickel chloride bath. Pulse plating allows nickel ions to diffuse into the interior of the forest during off portions of the cycle. Done properly, this solves the problem of the formation of an external crust which otherwise blocks Ni deposition in the interior of the structures. Thus, densities of 86$\pm$3% of bulk Ni for the composite structures are achieved. Cantilever structures do not yield under load but break. Measurements of the material properties of this composite material indicate an elastic modulus of approximately 42 GPa and a strength of 400 MPa. We demonstrate the utility of this method with a simple MEMS magnetic actuator consisting of a proof mass and two flexures. We achieved 7 mN actuation forces.

Keywords: Magnetic, carbon, microelectromechanical, nickel, aspect ratio

ACKNOWLEDGMENTS

The authors would like to thank the Brigham Young University Department of Physics and Astronomy and the Brigham Young University Office of Research & Creative Activities for financial support. The authors would also like to thank Andrew Davis and Ryan Badger, student researchers who did initial work with nickel plating.

Contents

Chapter 1

Introduction

1.1 MEMS

MEMS, micro-electro-mechanical systems, sensors and actuators are used in smart phones, automobiles, gaming systems, military equipment and a wealth of other applications. These small devices allow electronics to interface with physical world. For example, an acceleometer is a device that senses physical acceleration. Cell phones and video game controllers use accelerometers to interact with the user. Figure 1.1 is a basic layout of how one of these devices might work. Here the frame is keep ridged and a movable proof mass is attached by to thing flexures. As the proof mass experiences a force or acceleration it will displace relative to the frame. This displacement can be measured optically or by the changing capacitance between the proof mass and the frame.

In these devices, high-aspect-ratios (HAR) are often desirable. HAR refer to objects that have a length or width that is much smaller than their height, for example a sky scrapper has a high-aspect-ratio. In MEMS devices, HAR increase mechanical robustness and surface area for capacitive actuation and sensing, while decreasing the out-of-plane motion and, consequently, the

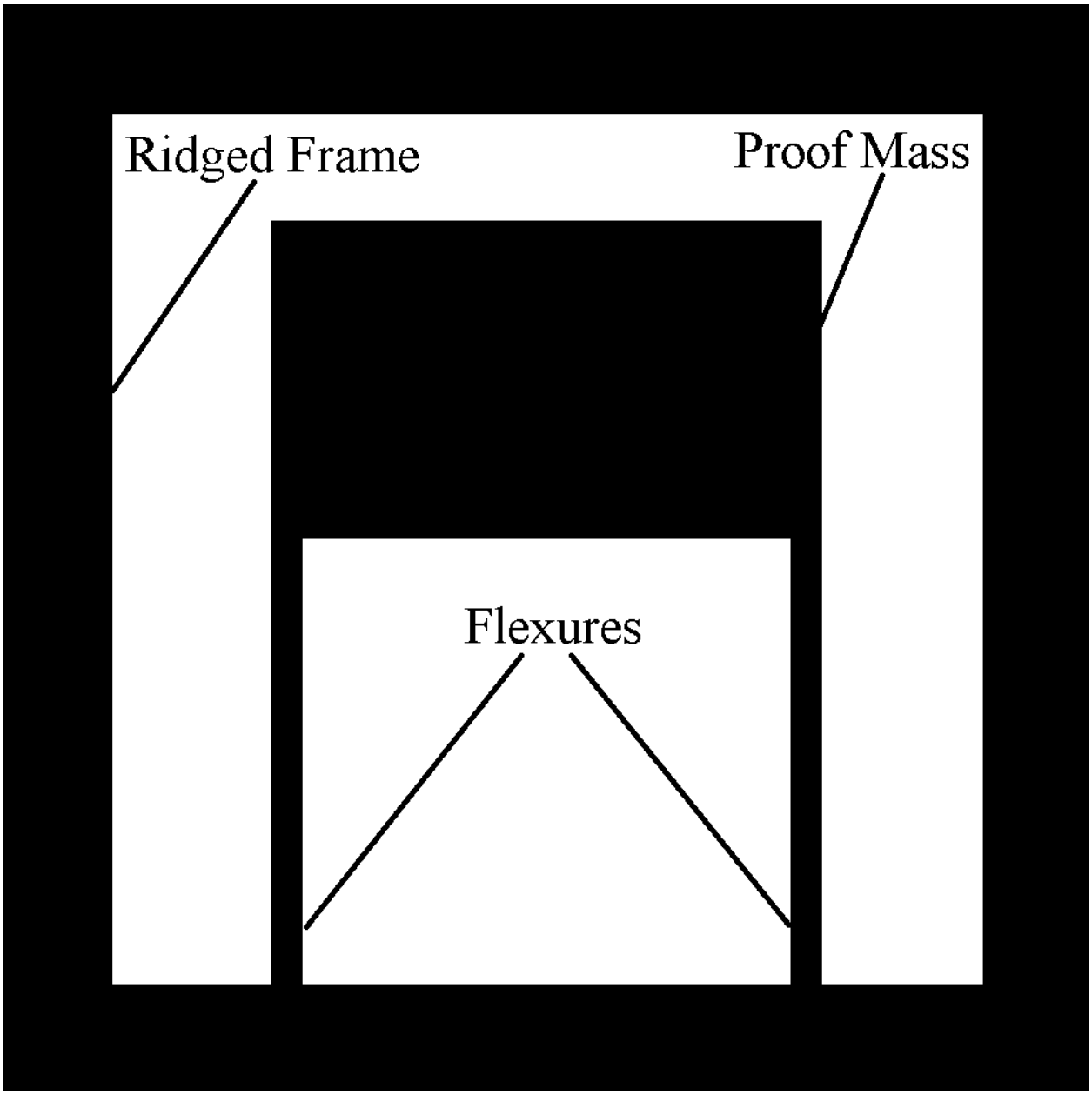

Figure 1.1 Layout of a simple MEMS actuator or sensor. The proof mass deflects as it experiences a force. This motion could either be used to preform a task or measured to calculate acceleration.

crosstalk of these devices [1]. Consequently, devices with HAR are more powerful other MEMS devices. Methods for fabricating high-aspect-ratio structures include: subtractive processes such as deep reactive ion etching (DRIE) [2], additive processes, such as LIGA [3] and carbon nanotube templated microfabrication (CNT-M) [4]. Even though each of these processes have been somewhat successful in fabricating high-aspect-ratio microstructures, creating similar structures from metals remains a challenge (with the exception of titanium, which has found success using DRIE [5]).

Metal MEMS advantages include: high density, high yield strength, high yield strain, as well as high thermal and electrical conductivity. Each of these properties enables higher performance for MEMS devices. Additionally, ferromagnetic metals can enable actuation devices that are not currently possible. Presently, most actuation is done capacitively or by piezoelectric materials [6]. Magnetic actuation can achieve larger forces at larger distances. Magnetic actuation forces begin to be stronger than capacitive forces at distances above about 2 μm [7], and magnetism can be used to actuate devices at millimeter or even centimeter distances. Consequently, applications can be envisioned in which a single external magnet or electromagnet can be used to actuate several devices simultaneously.

1.2 Current Technology

LIGA has been the most successful method for fabricating metal MEMS [3]. It uses synchrotron radiation to expose a high-aspect-ratio photoresist. After the resist is developed, the holes are filled via electroforming, a special version of electroplating designed to deposit thicker layers. The drawbacks of this process are the synchrotron expense [3], the difficulties of electroforming, voids

in the deposit [8], and nonuniform thickness of deposits [9].

1.3 Our Technology

Here, we show CNT-M can be extended to metals, and that it addresses some of the disadvantages of LIGA. In CNT-M, vertically aligned carbon nanotube (CNT) forests are grown from a patterned iron catalyst. The process is like extruding a 3D structure from a 2D pattern. The CNT forest grows into a MEMS geometry but has no structural integrity. As a result, it is infiltrated and filled with another material by CVD (chemical vapor deposition) [4]. Others have successfully infiltrated forests with carbon, silicon nitride and amorphous silicon [4, 10], but attempts to infiltrate with metals by CVD have met limited success [11, 12].

We successfully infiltrated with metals by means of an electroplating process. The patterning in this process is significantly less expensive than LIGA because it can be done with standard photolithography. It also can be done at aspect-ratios greater than 20:1 (fig. 1.2) without significant voids. The secret to void-free infiltration is pulse deposition. The sticking coefficient is the probability that an adatom, an atom that is being deposited, deposits instead of rebounding off the forest. Using pulsed electroplating we can create a low effective sticking coefficient because ions will only deposit when there is sufficient potential applied to the forest to drive the chemical reduction of the nickel containing ion, depositing the metal.

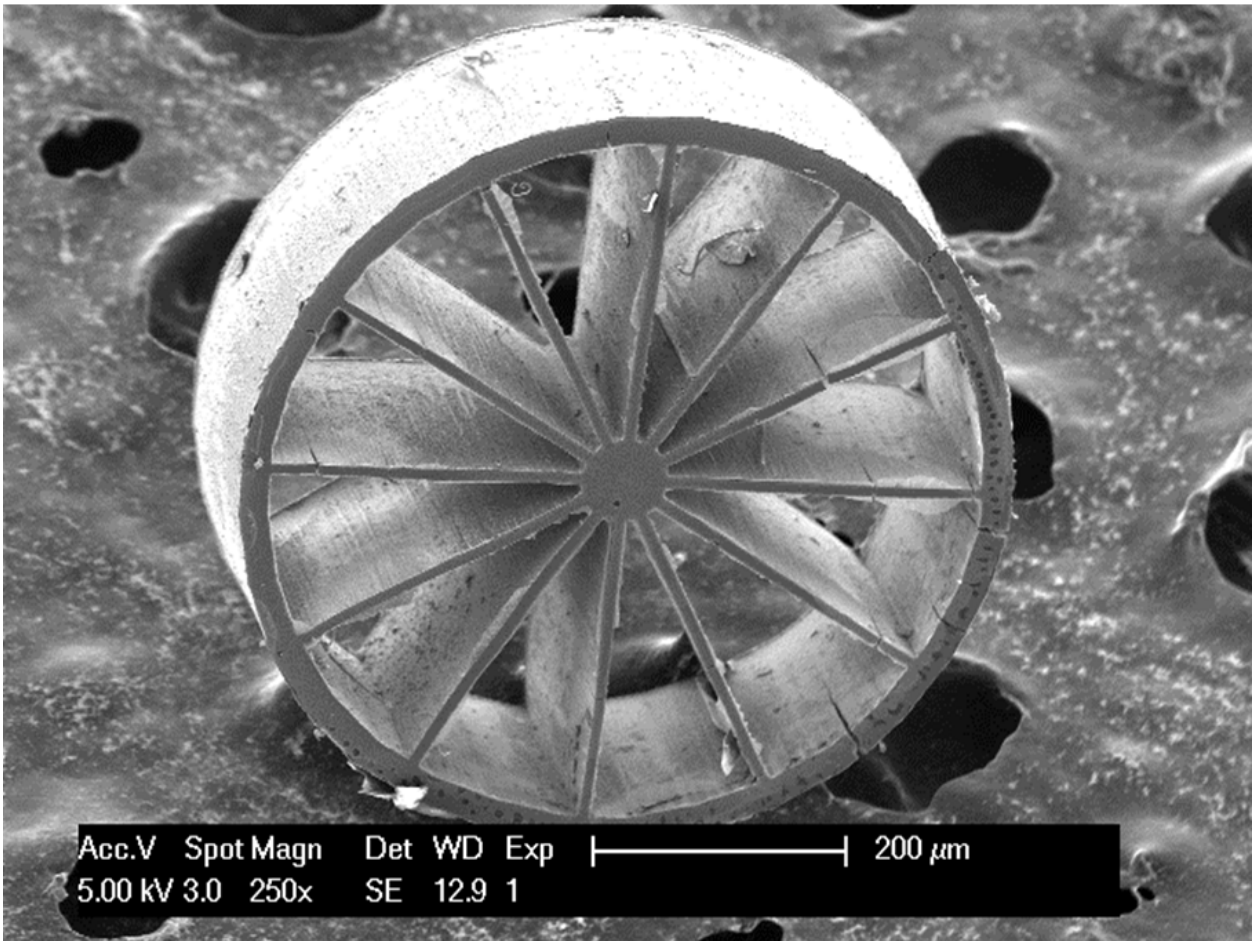

Figure 1.2 An SEM micrograph of a wagon wheel structure made by electroplating carbon-coated CNTs. The spokes are 10 μm wide and the wheel is over 200 μm wide.

1.4 Methods

1.4.1 Sample Fabrication

As seen in fig. 1.3, the process outlined by Hutchinson et al. was followed to prepare the samples for electroplating [4]. Silicon wafers were coated in 30 nm of Al_2O_3. Photoresist was then patterned on the wafer via contact photolithography. A 7 nm layer of iron (Fe) was thermally evaporated on the wafer, and the photoresist was subsequently stripped by sonication in NMP, leaving behind a patterned layer of Fe which served as the catalyst for CNT growth [10]. The next two steps were performed in the same deposition tube. First, vertically aligned CNTs were grown by CVD. The sample was placed in a 7/8 in. ID tube furnace, heated to 750 °C. Then, 220 sccm of H_2 was flowed while the furnace was heated to reduce the catalyst. After the furnace reached 750 °C, H_2 flow was continued at the same rate and 260 sccm of C_2H_4 was added. Since the resulting CNT structures are weak and can deform in the electroplating bath, a thin nanocrystalline carbon layer was deposited. This was done immediately after CNT growth by increasing the temperature to 900 °C for two minutes while continuing the same gas flow rates. An SEM micrograph showing typical CNT forests before and after carbon coating can be seen in fig. 1.4.

1.4.2 Electroplating

After the forests were grown and strengthened, they were filled with nickel by pulse electroplating. The electroplating must be tuned to avoid there being more deposition on the wafer than at the substrate, as seen in fig. 1.5. It is suspected that this nonuniform deposition occurs because the electroplating depletes the metal ions from the solution faster than they can be replenished by diffusion. To increase diffusion, both the composition of the bath and the rest time in between plating pulses were changed. An aqueous $NiCl_2$ solution was found to enable sufficiently rapid diffusion. The solution was composed of 125 g/l $NiCl_2$ $6H_2O$ (as nickel(II) chloride hexahydrate) and 12.5

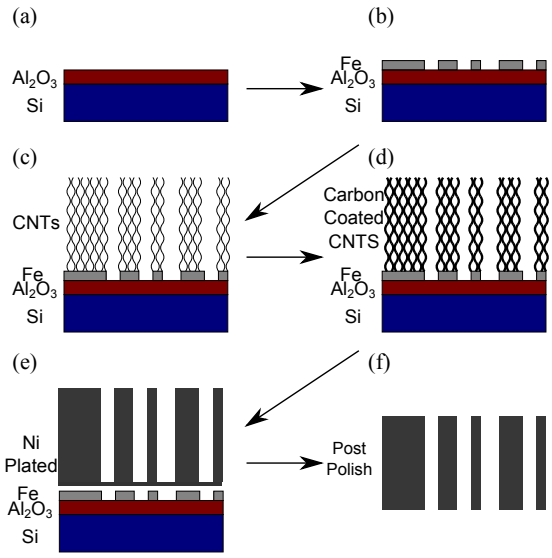

Figure 1.3 Process diagram for nickel CNT-M (a) A 30 nm layer of Al_2O_3 is e-beam evaporated on a silicon wafer. (b) Liftoff is used to produce a patterned 7 nm Fe layer. The Fe serves as catalyst for CNT growth. (c) Vertically aligned CNTs grow from the Fe catalyst. (d) They are coated with a thin (approx. 20 nm) layer of nanocrystalline carbon by atmospheric pressure CVD at 900 °C. (e) The forest is electroplated with Ni until it is filled. The electroplating usually causes the structure to detach from the wafer. If it did not detach, it was released by etching in 30% KOH. (f) A thin floor layer forms on the wafer during plating. The layer is removed by mechanical polishing with a 3 μm lapping film.

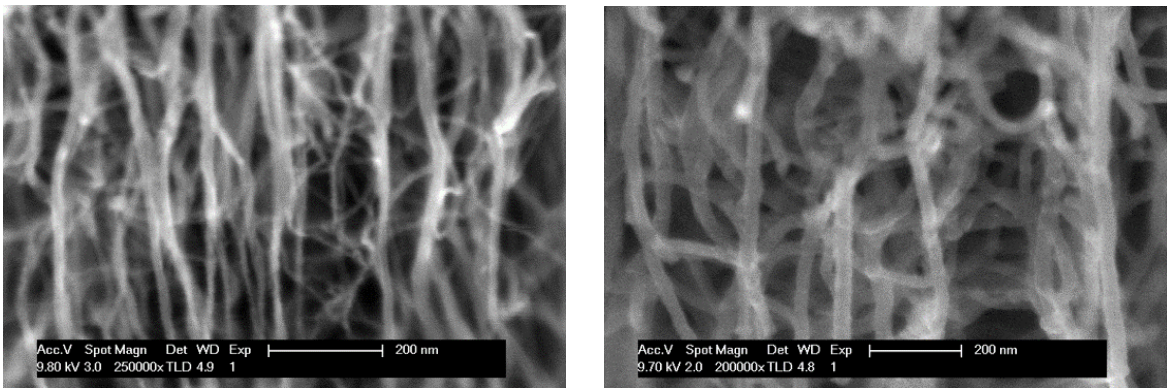

(a) **(b)**

Figure 1.4 SEM micrographs of typical (a) vertically aligned CNTs and (b) carbon coated vertically aligned CNTs.

g/l boric acid.

Current per area is the traditional measure of current density, but it is a difficult metric to use with CNT forests. Measuring the surface area of a CNT forest is not trivial. Furthermore, this measurement does not remain constant throughout the plating process. As metal is deposited on the CNTs the surface area will rise initially and then fall as the deposits grow together. The better metric in this case is current per unit volume. All of the samples were plated with 8 A/cm^3 during the on cycle.

Prior to electroplating, the samples were treated with ozone. Because carbon coated CNTs are hydrophobic, air can become trapped in the forest during insertion into the plating bath. This trapped air results in voids (fig. 1.6). Ozone treatment has been shown to change CNTs from hydrophobic to hydrophilic [13]. The samples were ozonated following the procedure outlined in Jensen et. al for at least 30 min [14].

Electrical contact was made to the sample by touching the top of the carbon coated CNTs with a needle point. After being placed in the solution, the forest was left to sit for 30 min before plating began. During plating, the on cycle was 3 ms and the off cycle was 27 ms, unless otherwise noted. Plating continued for 8.5 hours. The solution was maintained at 50 °C and stirred with a magnetic stir rod. The nickel source was sulfur depolarized nickel discs kept in a titanium basket.

1.4.3 Floor Layer

As discussed in Moulton et. al [10], during CNT growth thin beams grow straighter and with more consistent dimensions when there is a nearby CNT guide structure which is also growing [10]. Guide structures were placed 20 μm from the thin beams on the device grown here. While they were not attached to the sample before plating, they became attached during the plating process.

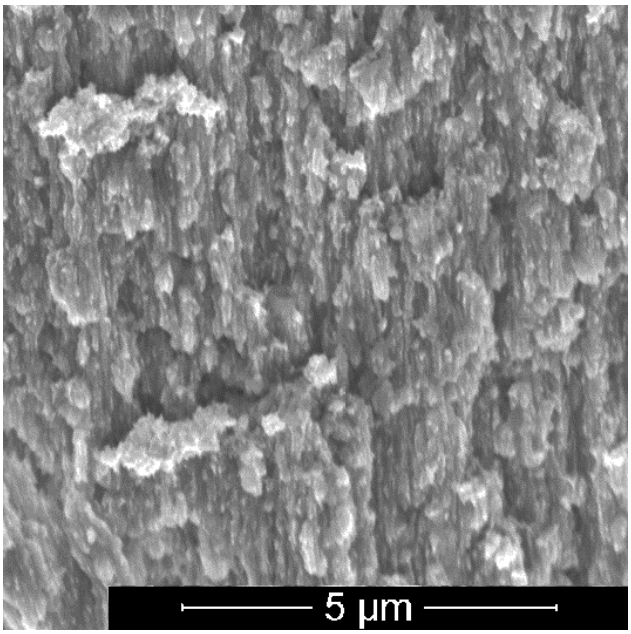

(a)

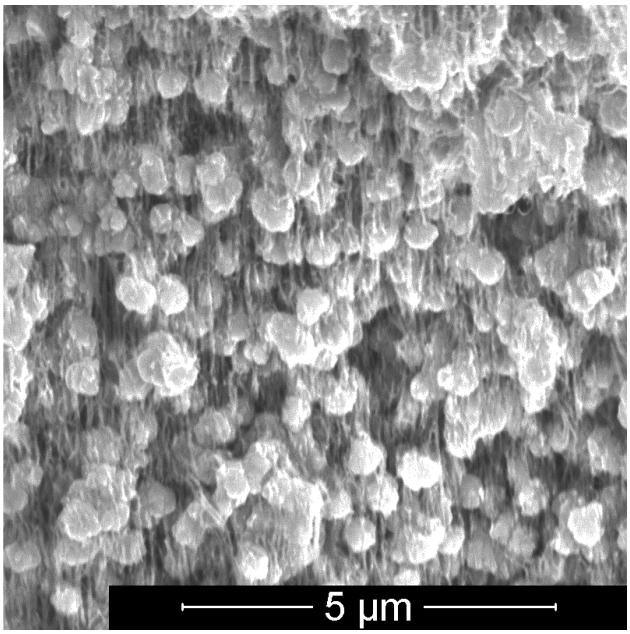

(b)

Figure 1.5 SEM micrographs of the cross-section of the interior (broken open) of an electroplated CNT structure (a) near the top of the sample (b) near the bottom of the sample and the substrate. The structure is over 200 μm tall. It was plated in a $NiCl_2$ bath at 8 A/cm^3 and a 3 ms on time, but the off time was only 6 ms. It can be seen that there is significantly more nickel deposited near the top, but little near the bottom. This is most evident from the CNTs being visible near the bottom, but not near the top.

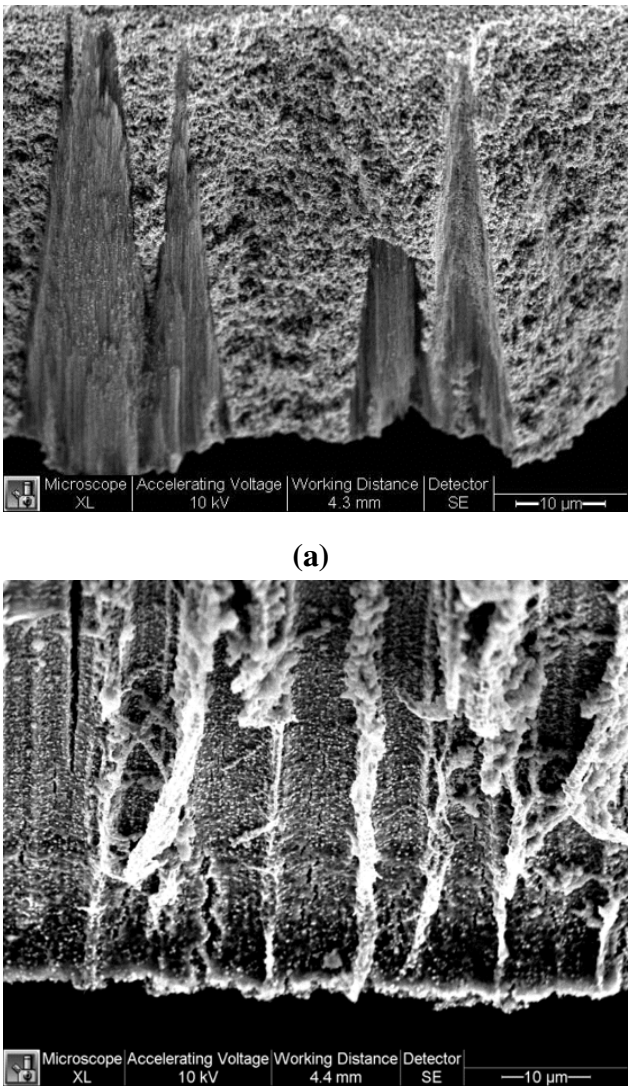

(a)

(b)

Figure 1.6 SEM images of a nickel plated CNT forest's cross section with (a) and without (b) ozone treatment. The conically shaped voids disappear when the carbon coated CNTs are treated with ozone. We suspect it is because the ozone makes the forest hydrophilic.

During the CVD carbon coating step, a thin layer of conductive carbon was deposited onto the wafer. Nickel deposits both onto this layer and the CNTs, attaching the guide structures to the beams. To remove this thin attachment layer, the sample was polished with a 3 μm lapping film. During the polishing the sample was attached to a piece of glass with cyanoacrylate glue to prevent the beams from breaking. After the floor layer was polished away the sample was allowed to soak in acetone until the glue dissolved, releasing it from the glass.

This step is not ideal for manufacturing, but there is potentially an alternative. If the samples are grown on a thicker insulating layer and the conductive carbon layer is removed, possibly by O_2 plasma etching, the nickel will not deposit on the substrate because there will be no electrical contact to the substrate. This would render the polishing step unnecessary.

Additionally, it is worth noting that at one point we attempted to make electrical contact to the structure by contacting this conductive floor layer instead of contacting the structure directly. This resulted in a forest that deposited well near the wafer but did not plate well near the top of the structure as seen in figure 1.7.

1.5 Material Properties

The structure is largely comprised of nickel; however, the resulting composite material also contains carbon-coated CNTs and some voids. To better understand this composite material for potential uses in MEMS, measurements were made to determine three material properties: density (ρ), elastic modulus (E), and tensile strength (σ).

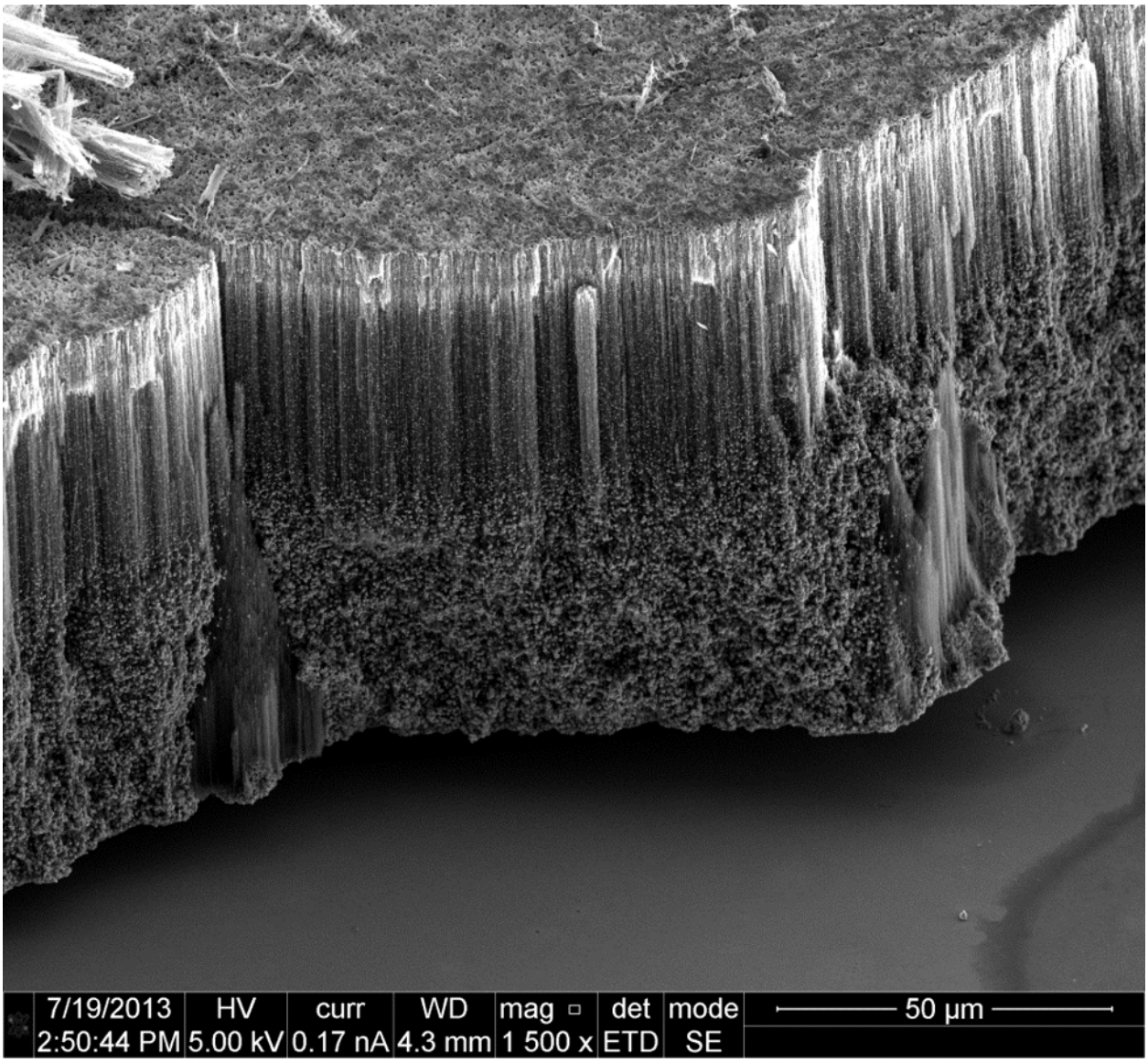

Figure 1.7 SEM images of the cross section of CNT forests with electrical contact made to the carbon layer that forms on the silicon layer during the carbon coating of the CNTs.

Several fixed free cantilever beams were fabricated. The force vs. deflection curve was measured using an Instron tabletop tensile testing machine in a manner similar to the methods described in Hanna et. al [15]. Fig. 1.8 shows the force-deflection curves for 3 cantilevers of different lengths. It should be noted the material does not yield prior to breaking. Consequently, references to tensile strength refer to ultimate and not yield, strength. The elastic modulus and strength was calculated from these curves. The slope of the curve (k) relates to the elastic modulus as shown [6]:

$$E = \frac{4L^3k}{WH^3} \tag{1.1}$$

where E is the elastic modulus and L, W, and H are the length, width, and height respectively of the cantilever beam. Measurements of the elastic modulus ranged from 20-65 GPa with an average value of 42.4 GPa. Microfabricated nickel from other processes generally has a modulus of about 200 GPa, meaning our structures are significantly more compliant [16, 17]. The tensile strength can be obtained from the force on the beam at breaking and the beam's dimensions [6]:

$$\sigma = \frac{6FL}{WH^2} \tag{1.2}$$

where F is the force when the beam broke. The strength values ranged from 229-643 MPa. The average value was 383 MPa. It should be noted eq. 2 does not take into account stress concentration which could be quite high because the radius of curvature between the cantilever and the base was less than 10 μm. As a result, the material's tensile strength may be significantly higher. The density was obtained by combining mass and volume measurements. The measured values ranged from 7.3-7.98 g/cm^3. The average value was 7.65 g/cm^3. This is 86% of the density of bulk nickel (8.9 g/cm^3).

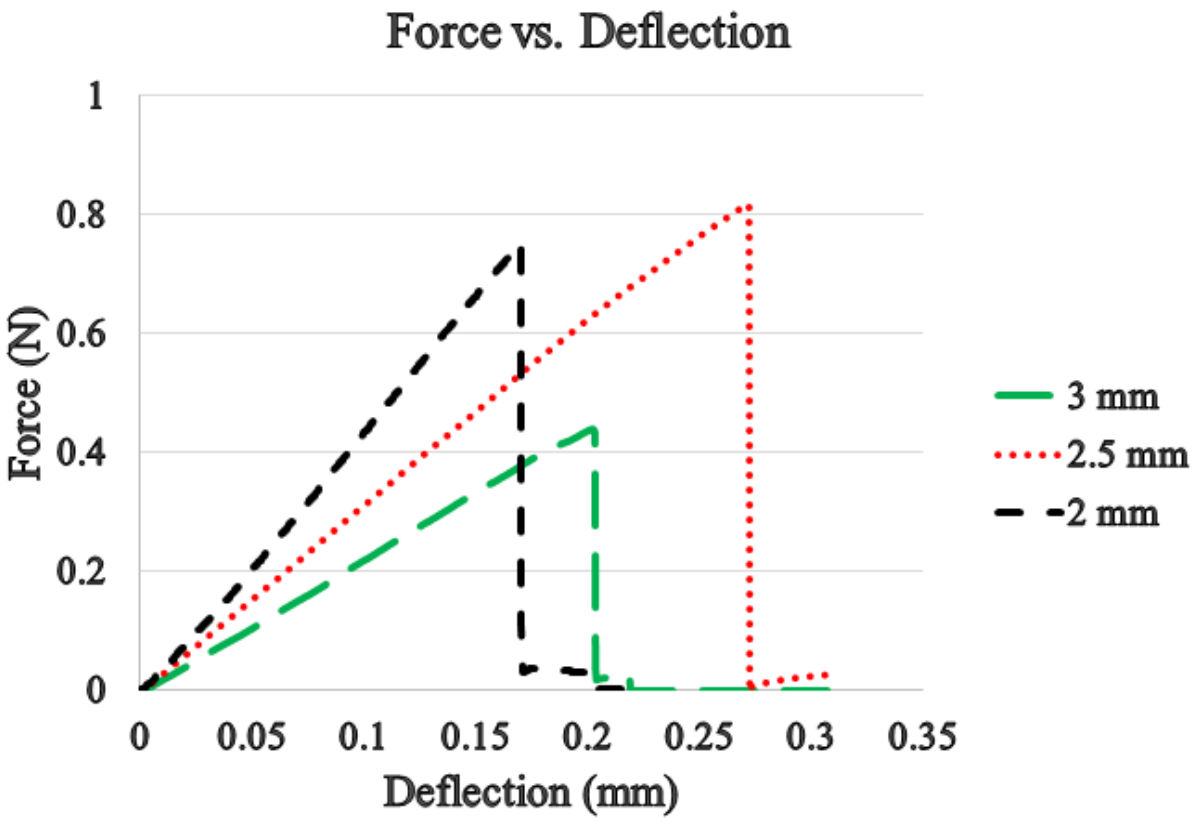

Figure 1.8 Force vs. deflection curves for three cantilevers of different lengths. The cantilevers were 190 μm tall and 525 μm wide. It should be noted the material does not yield prior to breaking.

1.6 Simple Device

To demonstrate the utility of this method, a simple MEMS device was constructed. The device consisted of a ridged frame connected to a floating proof mass by two 10 μm cantilever beams. This device imitates the basic function of a magnetic actuator. Several of these devices were fabricated. One example is shown in fig. 1.9. These devices have beams that are 1 mm long, 80 μm tall and 10 μm wide. One of the devices was cut open with a focused ion beam to show the interior (fig. 1.9). The cross section does not show any major voids confirming the high densities measured.

Two measurements were made on these devices. First, a neodymium magnet was brought within 2-3 mm of the device as seen in fig. 1.9. The proof mass deflected approximately 80 μm. Second, a Instron tabletop tensile tester was used to measure the force vs. deflection curve of another device with approximately the same dimensions. It can be seen the force the magnet needed to exert to achieve a displacement of 80 μm is 7 mN (fig. 1.9c).

1.7 Conclusion

High-aspect-ratio nickel microstructures can be fabricated using the CNT-M process. Aspect ratios greater than 20:1 can be achieved. Initial measurements of the material properties of this composite material indicate an elastic modulus of approximately 42 GPa, a strength of 400 MPa, and a density of 7.65 g/cm^3. A simple MEMS device consisting of a frame connected to two cantilever beams and a free standing proof mass was fabricated. The proof mass was deflected by bringing a magnet near the device. The magnetic force was found by measuring the force vs. deflection curve for the device. The force generated by the magnet in this case was 7 mN. This technology enables previously impossible applications in magnetic actuation because it allows fabrication of thicker

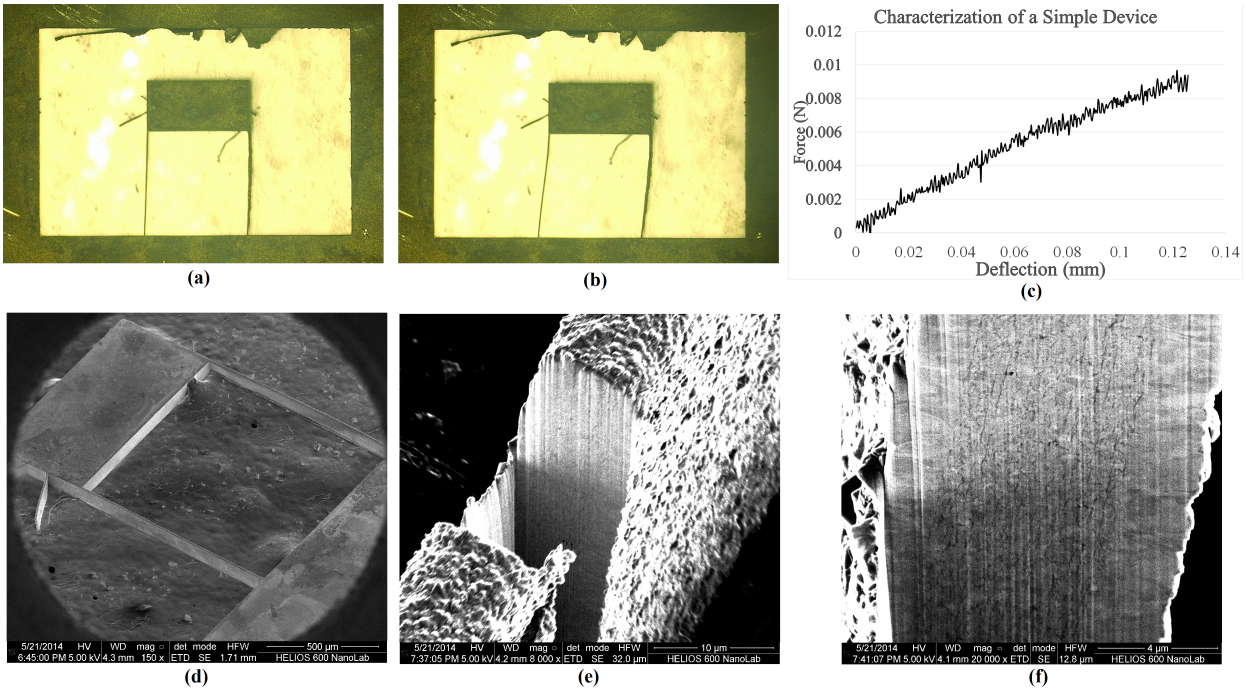

Figure 1.9 Characterization of a simple device: Optical microscope images of the device (a) undeflected and (b) deflecting towards a neodymium magnet. The deflection was approximately 80 μm with the magnet 2-3 mm away. (c) force-deflection curve for the device. The force required to achieve a deflection of 80 μm is about 7 mN. (d) SEM micrograph of the device seen in figures a and b. The beams are approximately 80 μm tall, 10 μm, and 1 mm long. The structure is free standing the surface seen here is carbon tape for imaging. The extra pieces coming off of the proof mass are connectors that were included to help with plating. They were removed mechanically with tweezers. (e) SEM micrograph of a beam that has been milled with a focused ion beam. The lack of large voids qualitatively confirms the density measurements. (f) Higher magnification micrograph of the same milled beam.

ferromagnetic structures capable of experiencing high magnetic actuation forces.

List of Figures

Bibliography

[1] S. W. Pang, "High-Aspect-Ratio Structures for MEMS," MRS Bulletin **26,** 307–308 (2011).

[2] E. H. Klaassen, K. Petersen, J. Noworolski, J. Logan, N. I. Maluf, J. Brown, C. Storment, W. McCulley, and G. T. Kovacs, "Silicon fusion bonding and deep reactive ion etching: a new technology for microstructures," Sensors and Actuators A: Physical **52,** 132–139 (1996).

[3] C. K. Malek and V. Saile, "Applications of LIGA technology to precision manufacturing of high-aspect-ratio micro-components and -systems: a review," Microelectronics Journal **35,** 131–143 (2004).

[4] D. N. Hutchison, N. B. Morrill, Q. Aten, B. W. Turner, B. D. Jensen, L. L. Howell, R. R. Vanfleet, and R. C. Davis, "Carbon Nanotubes as a Framework for High-Aspect-Ratio MEMS Fabrication," Journal of Microelectromechanical Systems **19,** 75–82 (2010).

[5] M. F. Aimi, M. P. Rao, N. C. MacDonald, A. Zuruzi, and D. P. Bothman, "High-aspect-ratio bulk micromachining of titanium," Nature materials **3,** 103âĂŞ105 (2004).

[6] C. Liu, in *Foundations of MEMS*, 2nd ed., A. Gilfillan and A. Dworkin, eds., (Prentice Hall, Upper Saddle River, NJ, 2012).

[7] D. Niarchos, "Magnetic MEMS: key issues and some applications," Sensors and Actuators A: Physical (2003).

[8] H. Wang, J. Tang, G. Li, C. Zhang, J. Zhu, Z. Wang, G. Ding, and X. Zhao, "A study on utilizing a chloride bath to electroform MEMS devices with high aspect ratio structures," Journal of Micromechanics and Microengineering **20,** 115024 (2010).

[9] H. Yang and S.-W. Kang, "Improvement of thickness uniformity in nickel electroforming for the LIGA process," International Journal of Machine Tools and Manufacture **40,** 1065–1072 (2000).

[10] K. Moulton, N. B. Morrill, A. M. Konneker, B. D. Jensen, R. R. Vanfleet, D. D. Allred, and R. C. Davis, "Effect of iron catalyst thickness on vertically aligned carbon nanotube forest straightness for CNT-MEMS," Journal of Micromechanics and Microengineering **22,** 055004 (2012).

[11] D. McKenna, "Tungsten Infiltrated Carbon Nanotube Forests As A Framework For 3-D Microfabrication," (2011).

[12] R. Hansen, "Mechanical and Electrical Properties of Carbon-Nanotube-Templated Metallic Microstructures," (2012).

[13] H. Wang, Z. Huang, Q. Cai, K. Kulkarni, C.-L. Chen, D. Carnahan, and Z. Ren, "Reversible transformation of hydrophobicity and hydrophilicity of aligned carbon nanotube arrays and buckypapers by dry processes," Carbon **48,** 868–875 (2010).

[14] D. S. Jensen, S. S. Kanyal, N. Madaan, A. J. Miles, R. C. Davis, R. Vanfleet, M. A. Vail, A. E. Dadson, and M. R. Linford, "Ozone priming of patterned carbon nanotube forests for subsequent atomic layer deposition-like deposition of SiO2 for the preparation of microfabricated thin layer chromatography plates," Journal of Vacuum Science & Technology B: Microelectronics and Nanometer Structures **31,** 031803 (2013).

[15] B. H. Hanna, W. C. Fazio, J. D. Tanner, J. M. Lund, T. S. Wood, R. C. Davis, R. R. Vanfleet, and B. D. Jensen, "Mechanical Property Measurement of Carbon Infiltrated Carbon Nanotube Structures for Compliant Micromechanisms," Journal of Microelectromechanical Systems **PP,** 1–1 (2014).

[16] H. Majjad, S. Basrour, P. Delobelle, and M. Schmidt, "Dynamic determination of Young's modulus of electroplated nickel used in LIGA technique," Sensors and Actuators A: Physical **74,** 148–151 (1999).

[17] S. Spearing, "Materials issues in microelectromechanical systems (MEMS)," Acta Materialia **48,** 179–196 (2000).

Index